

Laser-scanning of induction-melted Al alloys: are they representative of additively manufactured ones?

Authors: Zhaoxuan Ge¹, Sebastian Calderon¹, S. Mohadeseh Taheri-Mousavi^{1,2*}

¹Department of Materials Science and Engineering, Carnegie Mellon University, 5000 Forbes Avenue, Pittsburgh, PA 15213, USA.

²Department of Mechanical Engineering, Carnegie Mellon University, 5000 Forbes Avenue, Pittsburgh, PA 15213, USA.

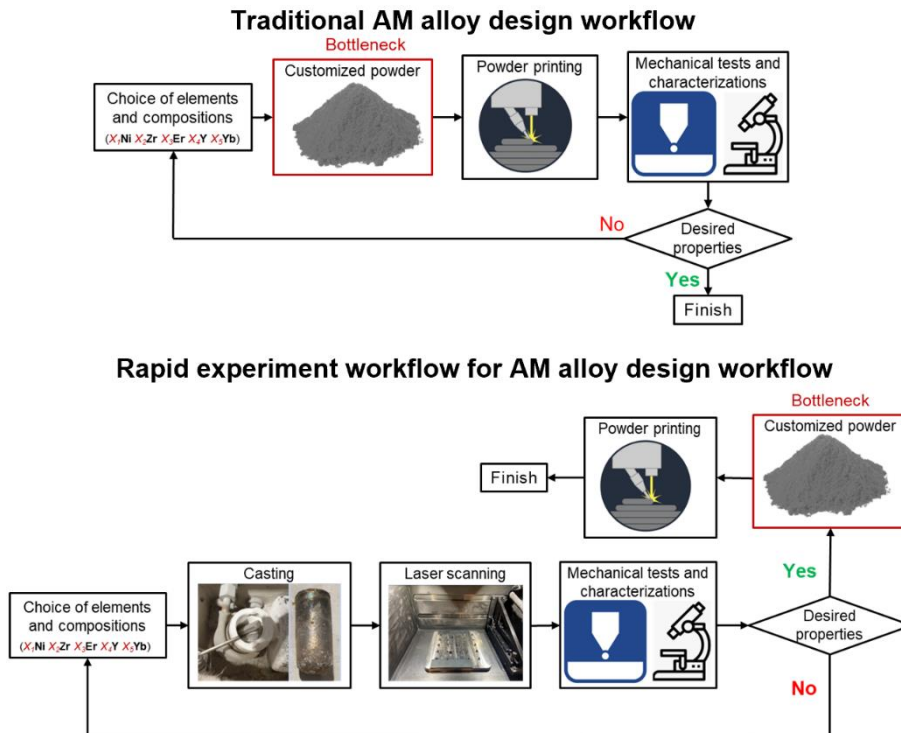
*Corresponding author: S. Mohadeseh Taheri-Mousavi,
smtaherimousavi@cmu.edu

Highlights:

- Compared microstructures and hardness of laser-scanned cast samples with LPBF ones.
- Microstructure is similar at high magnification, with phase size difference under 15%.
- Hardness of the laser-scanned sample can relatively represent that of LPBF ones.

Abstract:

The bottleneck of alloy design for powder-based additive manufacturing (AM) resides in powder production—an expensive and extremely time-consuming process hindering the rapid closed-loop design iterations. This study analyzed an expedited experimental workflow, i.e., multipath laser scanning of induction-melted samples, to mimic rapid solidification of AM to serve as an alternative approach to down-select from the design space. Using Al-Ni-Zr-Er model alloy, we compared the microstructural features between the laser-scanned sample and the laser powder bed fusion (LPBF) one. Our results showed that the microstructure morphology is the same for both samples. SEM-EDS ($< \times 12000$ magnification) shows differences in Zr and Er distribution justified by the repeated reheating for additional layers in the 3D-printed sample. Nonetheless, phase distribution was nearly the same at a high magnification scale demonstrated by STEM-EDS ($\geq \times 80000$). Phase sizes were also compared – the laser-scanned sample resembles 3D-printed with an average size difference of 15% in Al grain, 14% in Al-Ni-Er ternary precipitates, and 4% in L_{12} nanoprecipitates. Cooling rates for the two samples were estimated by Rosenthal equation, where the higher value of the 3D-printed sample compared with that of the laser-scanned sample explains its slightly finer phases. The mechanical properties of the two samples were evaluated by microhardness tests. The hardness of the laser-scanned sample was found to be 21% less than that of the 3D-printed sample. The potential reasons were discussed. The study also showed that a similar difference in hardness was observed when the experiments were repeated on a printable benchmark Al alloy showcasing only 1% absolute error. Thus, laser-scanned samples can serve as a relative predictor of the hardness of LPBF samples, and their highly similar microstructure at high magnification allows their applications in rapid screening tests.



Keywords: closed-loop alloy design, LPBF, multipath laser scanning, thermal history, microstructure, rapid experimental workflow

1. Introduction:

AM has major advantages of shortening supply chains for market distribution and realization of intricate geometric components. However, our current understanding of the underlying physical processes of AM is still limited. The community is still predominantly focusing on replicating reliable properties of cast/wrought alloys for AM parts. Despite these limitations, the inherent characteristics of AM pave a new pathway for alloy design. For example, the layer-wise fabrication of AM exhibits the capability to circumvent the occurrence of macrosegregation when incorporating heavy elements into the material matrix. Furthermore, LPBF as one of AM techniques has 10^5 - 10^7 K/s high cooling rates [1], which encompasses advantages including supersaturation of solutes [2], [3], [4], refinements of microstructural characteristics [5], [6], [7], [8], [9], augmentation in the volume fraction and/or number densities of strengthening phases [10], [11], and the ability to harness phase metastability [11], [12], [13]. These attributes offer a realm of design flexibility, fostering opportunities for innovative alloys that can unleash the economic potential of AM beyond the realm of prototyping.

To design a new alloy with AM, the process starts with the choice of the alloying elements and their concentrations. This choice can be made by performing e.g., calculation of phase diagram (CALPHAD)-based simulations. Upon identification of a specific composition, we make the customized powder and print them. Then, an array of characterization and performance evaluations are conducted to validate desired properties. Upon successful attainment of the target properties, the alloy design process concludes. However, the design usually requires several iterations to discover the optimal composition because of the difficulty in satisfying multiple metrics, which can be mutually exclusive. There are also uncertainties between numerical predictions and experimental validations. Among all the steps in the design loop, the critical bottleneck is in the production of custom powders [14]. This entails several steps, beginning with the ordering of ingots from vendors and awaiting their delivery. For those lacking atomization resources, the ingots must then be sent to another company for powder production. Once the custom powder is fabricated, a protracted process ensues for receiving and safely storing the powder, given powder's flammable and explosive characteristics. These procedures not only incur significant costs but also entail an extremely long lead time. It is noteworthy that sometimes the powder processing does not lead to the exact expected concentration of elements or lead to additions of external elements in the composition. Finally, some machines do not accept the production of low amounts of powders due to service challenges.

Considering the limited availability of the customized powder, high-throughput experiments such as the direct printing of chemical gradients within the specimen have been proposed to expedite the alloy design in the AM field [15], [16], [17], [18]. However, gradient printing is only applicable to certain technologies such as direct energy deposition (DED) [19], [20], [21] and ink jetting [22]. Even though the compositional gradient printing technique aims to generate integrated specimens that encapsulate substantial information from limited samples, powder production is still a necessity. In response to this challenge, an expedited experimental workflow has been introduced to mimic the rapid solidification of AM by laser scanning cast/induction melted alloys [13]. If the laser-scanned cast samples could be representative of the 3D-printed samples, compositions can be selected in an expedited and inexpensive way without powder production. We thus effectively move the bottleneck step out of design iteration (see

graphical abstract), i.e., the powder is only ordered if the composition is validated after several iterations on laser-scanned samples.

In this paper, we study how much laser-scanned samples are representative of AM samples in a model alloy, presenting their differences and similarities. It is noteworthy that we will not study intricacies of the laser-microstructure interactions within AM. Such a broad assertion requires further investigation, including an examination of thermal history, melt pool geometries, and their interactions under varying laser parameters on different alloys. Extensive research [23], [24], [25], [26], [27], [28], [29] has already been conducted on single-track laser scans, with and without powder, to discern similarities and discrepancies in thermal history and melt pool behavior on different alloys. It is expected that these problems could be more complex for multi-path laser scans. In this study, we focus on one set of laser parameters that enables maximum sample density to study if laser-scanned samples are representative of the 3D-printed ones. Special emphasis is placed on understanding to what extent the microstructures and strength of laser-scanned samples resemble the AMed ones. This is explored in great depth with the aid of multi-scale scanning electron microscopy (SEM), transmission electron microscopy (TEM), and scanning-transmission electron microscopy (STEM) characterizations. We expect this study to demonstrate the opportunities and limitations of the expedited experimental workflow for a model Al-Ni-Zr-Er alloy system while encouraging a broader investigation into the various laser parameters and different alloy systems in following studies.

2. Material system

In this study, an Al-Ni-Zr-Er model alloy, designed in our earlier study is used [13]. The alloy was designed for high-temperature (250°C) applications. It showcases a great coarsening resistance demonstrating stable yield strength and microstructure after aging 48 hours at an elevated temperature of 400°C. The yield strength is 400 MPa at a peak aging time of 8 hours at 400°C. ThermoCalc software was employed to simulate the material system. Specifically, Scheil calculation was conducted to comprehend the solidification process and simulate the as-built system, while a single equilibrium calculation was performed to simulate the material system under service conditions at 250°C. Fig. 1 illustrates the Scheil solidification curve of this alloy.

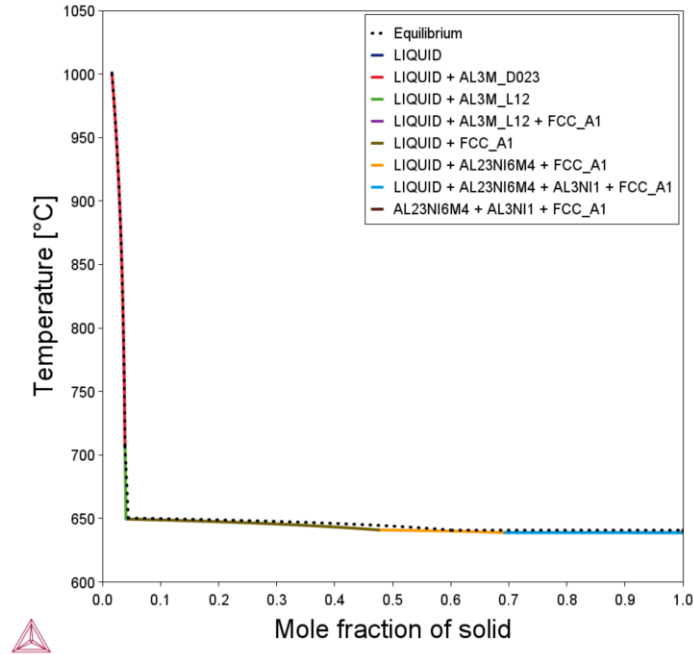


Fig. 1 Phase evolution during solidification of the Al-Ni-Zr-Er material system calculated from a Scheil calculation with ThermoCalc software.

Moreover, Table 1 provides a summary of present phases and their corresponding phase fractions in both the as-built system (Scheil calculation) and the in-service system at 250°C (single equilibrium calculation). The alloy system consists of various phases, including Al-FCC, Al₃Ni, Al₃M (in L₁₂ structure and D023 structure), and Al₂₃Ni₆M₄ (M can be Zr or Er). It is noteworthy that the ternary Al₂₃Ni₆M₄ phase diminishes to 0 at the equilibrium state. This phenomenon occurs because the Al₂₃Ni₆M₄ is a metastable phase and undergoes a transformation into L₁₂ (initially absent in the as-built system) and Al₃Ni phases after an extended aging period.

Table. 1 Stable phases and phase fraction at as-built system (Scheil calculation) and in-service system (Single equilibrium calculation) simulated by ThermoCalc.

Stable phases	Phase fraction (%)	
	As-built system	250°C in-service system
Al ₃ Ni	2.682	5.32
Al ₂₃ Ni ₆ M ₄	3.142	0
Al ₃ M (D023)	3.846	2.29
Al ₃ M (L ₁₂)	0.173	3.31
Al-FCC	Balance	

This material system is primarily governed by two prominent strengthening mechanisms: grain boundary strengthening mechanism (Hall-Petch effect, Eq. 1) and precipitation strengthening mechanisms (Orowan strengthening, Eq. 2). In this material system, Al grain boundaries act as impediments to the motion of dislocations, thus contributing to the augmentation of material strength, a phenomenon described by Eq. 1:

$$\sigma_{HP} = \sigma_0 + \frac{K}{\sqrt{d}} \quad 1$$

σ_0 is the material constant for the frictional stress in Al lattice, d is the grain size, and K is the Hall-Petch coefficient depending on material systems. Orowan strengthening primarily stems from the presence of $L1_2$ nanoprecipitates and $Al_{23}Ni_6Er_4$ precipitates. When external forces are applied, these particles interact with dislocations, impeding their sliding and obstructing their forward advancement, thus, strengthening the material. The increased strength achieved through the mechanism of Orowan dislocation looping around these non-shearable precipitates is as shown in Eq. 2 [30] :

$$\Delta\sigma_{Or} = Q \frac{0.4Gb}{\pi\sqrt{1-\nu}} \cdot \frac{\ln(\frac{2\bar{R}}{b})}{\bar{\lambda}} \quad 2$$

where Q is the Taylor factor for Al matrix, G is the shear modulus, b is the magnitude of Burgers vector, ν is the Poisson ratio, $\bar{R} = \sqrt{\frac{2}{3}} \langle r \rangle$ is the mean planar precipitate radius ($\langle r \rangle$ is the precipitate mean radius), and $\bar{\lambda} = (\sqrt{\frac{3\pi}{4f}} - 1.64)\bar{R}$ is the mean planar distance between precipitates, in which we assume a homogenous distribution of spherical precipitates on a cubic grid [31]. Here f is the volume fraction of the precipitates. As the volume fraction of precipitates increases and their size decreases, the contribution of Orowan strengthening to the material system intensifies. However, there is a critical threshold to consider, where precipitates that are too small, particularly those below 2 nm in size [13], may allow dislocations to shear through them, thereby diminishing the overall strengthening effect. Therefore, the objective was to achieve precipitate sizes that are as small as possible while remaining above the 2 nm threshold. This balance ensures an optimal combination of strengthening mechanisms, maximizing material performance while avoiding the detrimental effects of excessively small precipitates.

3. Experiment Method

3.1 Laser-scanned induction-melted sample preparation

The alloy with Al-0.4Er-1Zr-1.33Ni at. % was melted employing the MC20V induction heating system from Indutherm. Granulated elements with diameters less than 5 mm were utilized, with each batch comprising 30 g of raw elements. Prior to melting, a boron nitride (BN) spray was utilized to coat the surface of the Al_2O_3 crucible, serving to minimize the interaction between the melting elements and the crucible. A vacuum environment of 0.1 mbar was applied to reduce oxygen levels, and to prevent oxidation, argon gas was introduced to fill the chamber. The temperature was then elevated to 1000°C to ensure complete material melting, which was maintained for 5 minutes. Subsequently, the molten material was allowed to naturally cool inside

the chamber after the heat source was turned off, shaping it into rod structures with approximately 60 mm in length and 15 mm in diameter.

These rods were further processed by rolling them into metal sheets through a series of 10 iterations, gradually reducing the rolling gap until achieving a thickness of 2 mm. During rolling, the samples were heated to 100°C to prevent edge cracking. Following rolling, a subsequent pressing operation was conducted to flatten the slightly bent sheets.

Subsequently, the metal sheets underwent laser scanning by using the LT30 LPBF system from DMG MORI. The system was equipped with a solid-state Nd: YAG laser source emitting at a wavelength of 1064 nm, with a maximum laser power of 1000 W. The focus laser beam has a diameter of 70 μm with a Gaussian distribution. The chamber was maintained under vacuum and flowed with argon gas at 1 atm pressure, with a purity of 4.6, ensuring oxygen content inside the chamber remained below 1000 ppm. The building plate was kept at room temperature, and to prevent adhesion of the metal sheet to the plate, the protective BN spray was applied. The scanning region measured 200 × 25 mm², with processing parameters optimized to minimize printing defects: a scan speed of 300 mm/s, a hatch distance of 170 μm, and a laser power of 400 W. A stripe-scanning strategy with an 8 mm vector length was employed. These processing parameters are summarized in Table 2, and the workflow of the laser-scanned sample production is depicted in Fig. 2.

Table. 2 Processing parameters of the 3D-printed and laser-scanned samples.

	3D-printed sample	Laser-scanned sample
Scan speed	1100 mm/s	300 mm/s
Hatch distance	120 μm	170 μm
Laser power	350 W	400 W
Powder thickness	50 μm	NA
Preheat	200°C	Room temperature

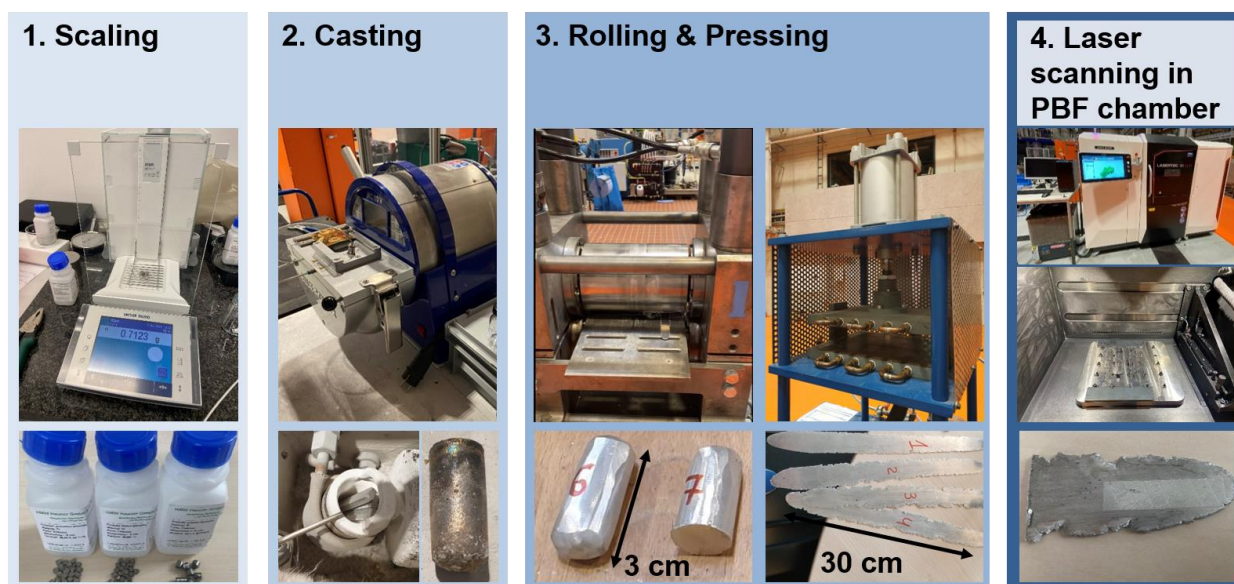


Fig. 2 Workflow for laser-scanned sample preparation. Above experiments and pictures were taken by Florian Hengsbach.

3.2 3D-printed sample preparation

The powder was generated through ultrasonic atomization using the AUS500 system from Indutherm Bluepower. The particle size was characterized using the laser diffraction method, revealing a distribution with $d_{10} = 44.5\%$, $d_{50} = 63.8\%$, and $d_{90} = 91.5\%$. The chemical composition of the powder was confirmed by X-ray fluorescence analysis.

Cubic samples measuring 6 mm in length were additively manufactured utilizing an SLM Solutions 250 HL machine. This system features a solid-state Nd: YAG laser operating at a wavelength of 1064 nm, with a maximum laser power of 400 W. The focus beam size is 70 μm with a Gaussian distribution. Before printing, the powder underwent vacuum drying to reduce the relative humidity to below 5%. The chamber was filled with Ar-4.6 to maintain an oxygen level below 1000 ppm to prevent oxidation. The build plate was heated to 200°C to facilitate adhesion. The processing parameters were optimized to minimize printing defects, including a laser power of 350 W, a hatch distance of 120 μm , a scan speed of 1100 mm/s, a layer thickness of 50 μm , a scan strategy involving 8 mm stripes, and a rotation angle of 67°.

These parameters are summarized in Table 2 and were compared with those used for the laser-scanned samples.

3.3 SEM characterization

SEM-BSE and SEM-EDS data were acquired using a ThermoFisher Apreo HiVac Scanning Electron Microscope, equipped with an EDAX Elite 150 SDD EDS detector. The SEM-EDS data were collected at 15-20 kV to detect the presence of all elements and to achieve fine spatial resolution for EDS mapping. The EDS spectra and maps were subsequently processed using the EDAX APEX software.

3.4 TEM characterization

Laser-scanned samples were prepared by mechanical polishing. Initially, the samples were polished using the Allied MultiPrep Polishing System to achieve a thickness of approximately 50 μm . Olympus SZX12 optical microscopy was employed to check the thickness. Subsequently, Ar-ion milling was carried out using the PIPS II system. The ion gun energy was set to 10 kV until pierced holes became visible. Thereafter, the energy was progressively reduced from 2 to 0.5 kV, until the desired thickness was obtained. Low-energy beam cleaning to reduce ion-induced damage was performed at an angle of 2° for a duration of 10 minutes for each energy. STEM images were acquired using a Thermo Fisher Themis 200 G3 instrument equipped with a probe aberration corrector. Images were captured at an accelerating voltage of 200 kV with a probe convergence semi-angle of 17.9 mrad. HAADF images were acquired using 70-200 mrad collection angles and drift-corrected using cross-correlation to reduce signal-to-noise ratio. EDS was acquired using a Thermo Fisher SuperXG2 detector, and the resulting data was processed using Thermo Fisher Scientific Velox software V3.6.0. Low magnification EDS data was collected with a probe current of 140 pA. A set of 211 frames were collected and drift-corrected using cross correlation. The data was post-filtered using the Gaussian method. Atomic-resolution EDS mapping was collected with a screen current of 130 pA. A set of 1465 frames was collected and drift-corrected using cross correlation.

For the 3D-printed sample analysis, the specimen was initially extracted using a Helios Nanolab 660 focused ion beam microscope manufactured by Thermo Fisher Scientific. A lamella of the targeted region was then isolated and affixed onto a molybdenum TEM grid using an Omniprobe 400 micromanipulator from Oxford Instruments. Subsequently, the sample was thinned by gradually reducing the ion beam voltage from 30 kV to 16 kV until the thickness reached 300 nm. The beam voltage was then halved until the thickness was further reduced to 150 nm. Finally, the sample underwent final polishing at 750 V until reaching a thickness of approximately 50 nm, utilizing a Model 1040 NanoMill from Fischione Instruments. The ion damage was cleaned with Ar-ion milling by Fischione 1051 TEM Mill from Fischione Instruments. The cleaning process involved using beam voltages of 0.3 and 0.1 kV for durations of 3 and 1 minute, respectively. Characterization of the sample was conducted using the Themis Z probe aberration-corrected TEM/STEM system from Thermo Fisher Scientific. STEM images were acquired at a voltage of 300 kV, a beam current of 40 pA, and a probe convergence semi-angle of 18.8 mrad. High-angle annular dark-field (HAADF) images were obtained using a collection semi-angle of 78-200 mrad with drift-correction implemented via the Revolving STEM method [32]. Energy-dispersive EDS analysis was performed using a Thermo Fisher SuperX detector, and the resulting data was processed using Thermo Fisher Scientific Velox software. Low-magnification EDS data was acquired using a beam current of 200 pA and

processed using a 5-pixel averaging filter. Atomic EDS data acquisition employed a beam current of 50 pA and was filtered using non-local principal component analysis [33].

3.5 Hardness test

Micro-hardness of the laser-scanned sample and 3D-printed sample were measured by Wilson VH3100 from Beuhler. For both samples, 10 measurements were performed under 100 g loading force, and the average hardness was taken. The indentation depth was calculated to ensure that the penetration is within the rapid solidification features, e.g., melt pool depth, of the laser-scanned sample. The indent of Vickers hardness is a standard 136° pyramidal diamond. The penetration depth was calculated from the square indent based on geometry as described by Eq. 3,

$$t = \frac{d/2}{\tan(136^\circ/2)} = 0.202 \cdot d \quad 3$$

where t is the penetration depth and d is the diagonal of the square indent.

3.5 Phase size measurement

Phase sizes were measured by applying *ImageJ* to the microstructure features acquired from SEM and TEM images. A line was drawn across the features, and the greyscale intensity of the drawn line was plotted against the length. Two high-intensity points corresponding to the edge of the features were taken, and the length difference between the two points was considered to be the phase size.

4. Results and discussion

SEM-EDS imaging was employed to analyze the microstructural characteristics of the 3D-printed and laser-scanned specimens, as depicted in Fig. 3. Both samples displayed dual-morphology microstructures comprising equiaxed grains (delineated by solid white contours) and eutectic lamellae (delineated by dashed white contours). A region that contains both microstructure morphologies was in the yellow dashed box and was magnified to clearly show lamellae and equiaxed grains of both samples (Fig. 3(a5) and Fig. 3(b5)). Initially, the eutectic lamellae were located within and partitioning the Al grains. As the material was aged, these fine lamellae coarsened and underwent a transformation into precipitates distributed along the grain boundaries, and the equiaxed Al grains appeared. The size of the equiaxed grains was measured, and the distribution is shown in Supplementary information. EDS mapping revealed the presence of micron-scale Zr-rich and Ni-rich large islands in both samples, indicative of Al_3Ni and Al_3Zr (D023) phases as suggested by CALPHAD simulations. Despite the general similarity, it is noteworthy to observe that the Zr-rich phase (Al_3Zr) in the laser-scanned sample exhibits larger dimensions compared to that in the 3D-printed sample (see Fig. 3(a3) and Fig. 3(b3)). One potential explanation for this phenomenon is that Al_3Zr grains in the as-cast induction-melted sample may reach sizes of up to hundreds of micrometers due to the slow cooling rate. Given that the beam diameter of the laser is only 70 μm , it is too small to fully remelt the entire phase. As a result, when the laser is passed over the sample, the phase sizes will largely remain as it was

in the original as-cast sample.

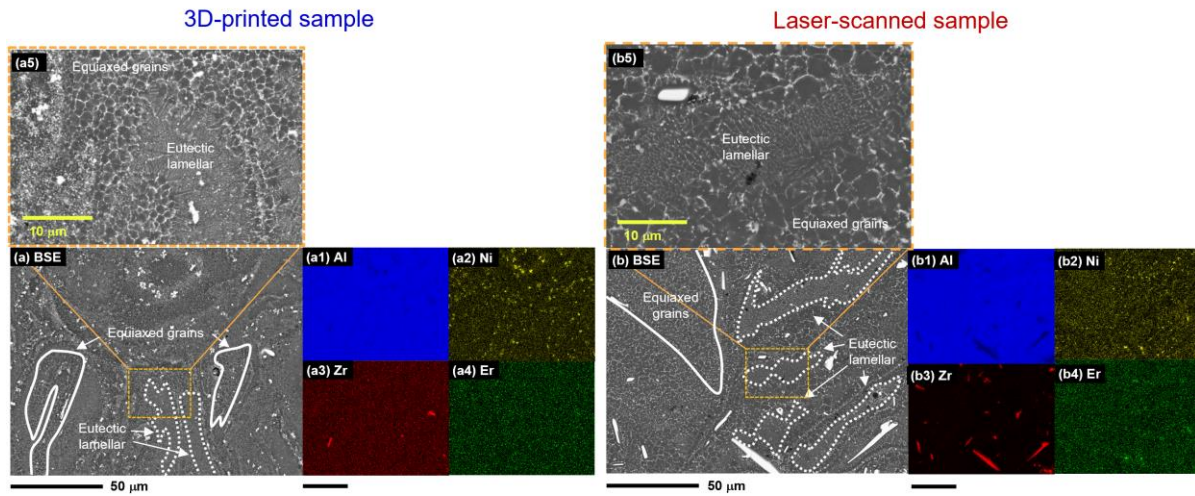


Fig. 3 SEM-EDS images of (a) 3D-printed sample and (b) laser-scanned sample. Both samples display a microstructural morphology characterized by eutectic lamellae and equiaxed grains. Zoomed-in images (a5 and b5) from the designated yellow boxes in the 3D-printed and laser-scanned samples, respectively, distinctly illustrate these two morphologies. EDS maps (a 1-4, b 1-4) reveal the presence of micron-sized Ni-rich and Zr-rich islands.

We then conducted SEM-EDS analysis at high magnification within the equiaxed regions of both samples as shown in Fig. 4. At this scale, we can still observe the presence of much smaller Ni-rich (Al_3Ni) and Zr-rich (Al_3Zr) precipitates in both specimens. Additionally, segregation of Ni and Er along grain boundaries was observed, particularly pronounced in the laser-scanned sample. These regions rich in Ni and Er are anticipated to correspond to $\text{Al}_{123}\text{Ni}_6\text{M}_4$ ternary precipitates predicted by CALPHAD simulations. Notably, this ternary phase is a metastable phase which is only associated with rapid solidification processes. Furthermore, examination of Fig. 4(a4) and Fig. 4(b4) reveals that the segregation of Er at grain boundaries is more pronounced in the laser-scanned sample than in the 3D-printed sample. These disparities may be attributed to the different processing for the two samples. In the case of powder printing, the layer thickness of 50 μm undergoes remelting as the subsequent layer of powder is melted. Consequently, a thermal cycling parallel to the printing direction induces additional thermal dynamic driving force, prompting metastable ternary phases segregated at the grain boundaries to transform into nanoscale L_{12} precipitates dispersed inside the Al grains. Besides, these L_{12} nanoprecipitates are too small to be resolved by SEM detectors. This results in a more uniform

distribution of Er throughout the material compared to the laser-scanned sample.

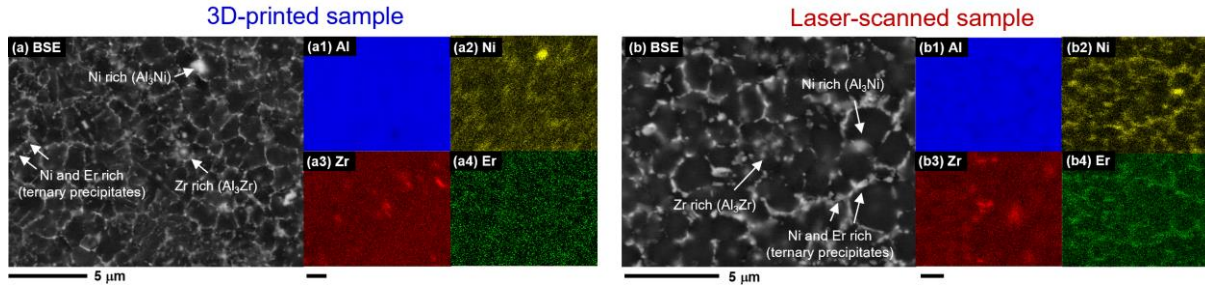


Fig. 4 SEM-EDS images of 3D-printed sample and laser-scanned sample. Equiaxed Al grains, Al₃Zr, Al₃Ni, and Al-Ni-Er ternary phases were observed in both samples.

To compare the microstructure in the local region, we further zoomed into one grain with STEM and performed EDS for both samples as shown in Fig. 5. At this grain-scale magnification, the microstructure and phase distributions of the two specimens appeared remarkably similar. Specifically, Al-Ni-Er ternary phases were observed to be distributed along the grain boundaries in both samples, consistent with the observations made through SEM-EDS analysis.

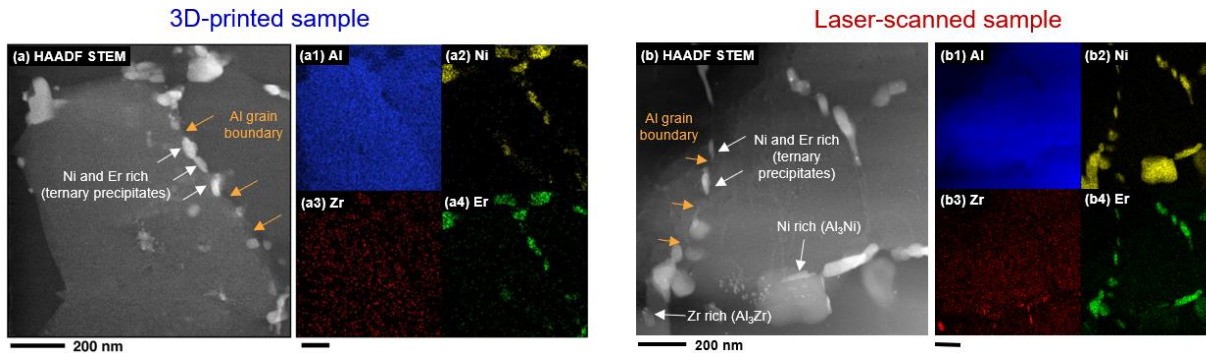


Fig. 5 Low-magnification STEM-EDS images of 3D-printed sample and laser-scanned sample. The Al-Ni-Er rich ternary phase is located on grain boundaries in both samples. The images of 3D-printed sample are from [13].

Upon closer examination of the Al grain interiors, L₁₂ nanoprecipitates were observed in the laser-scanned sample and 3D-printed sample as shown in Fig. 6. Coherent interfaces were observed between the L₁₂ nanoprecipitates and the Al matrix in both cases. Additionally, a core-shell-like structure was identified within the L₁₂ nanoprecipitates in both samples. This structure revealed a higher concentration of Zr in the shell, while Er was more concentrated in the core. This core-shell structure agrees to existing literature [34], [35]. The formation of the Zr/Er segregation in the core-shell structure was previously justified through first principal density functional theory (DFT) by Zhang et al [36]. The formation of the core-shell structure can also be elucidated by considering the lattice parameter of Zr exhibiting more similarity to that of the Al matrix, which makes it energetically favorable to the distribution in contact with the Al matrix. In this structure, the slower diffusion rate of Zr within the Al matrix at the shell effectively encapsulates the more rapidly diffusing Er within the core. This configuration enhances coarsening resistance, which explains the robustness of the material's strength even at

temperatures up to 400°C [37], [38], [39].

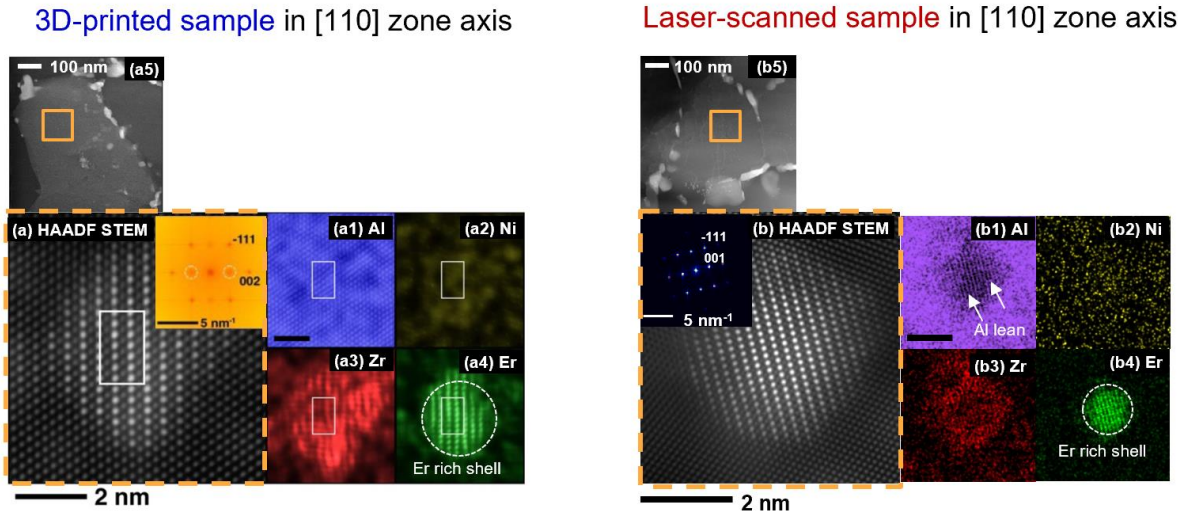


Fig. 6 Low-magnification STEM-EDS images of 3D-printed sample and laser-scanned sample. The Al-Ni-Er rich ternary phase is located on grain boundaries in both samples. The images of 3D-printed sample are from [13].

The quantitative analyses of phase dimensions are presented in Table 3. Notably, the L_{12} nanoprecipitates exhibit only 4% sizes difference across both samples, while the dimensions of Al grains and ternary precipitates in the laser-scanned sample exhibits a respective increase of 15% and 14% compared to those in the 3D-printed. This is contradictory to our expectation that the phase sizes were expected to be smaller in the laser-scanned sample. Since the laser beam was passed over the alloy sheet surface only once, in contrast to the 3D-printed sample, which experienced a cyclic thermal history parallel to the printing direction. The laser-scanned sample was anticipated to have less coarsened and thus smaller microstructural features due to reduced exposure to the heating source. However, the variance could be attributed to distinctions in cooling rates resultant from different processing parameters. The cooling rate, as a crucial factor to affect microstructural features, can be approximated using the Rosenthal equation [40] (Eq. 4), which characterizes the thermal profiles of a mobile point source which is related to the moving laser within the LPBF setup.

Table. 3 Phase size comparison between the two sample

	Phase size		
	Al grains (μm)	Ternary precipitates (nm)	L_{12} nanoprecipitates (nm)
3D-printed sample	1.37 ± 0.57	45.1 ± 6.7	2.5 ± 0.7
Laser-scanned sample	1.58 ± 0.55	51.6 ± 16.4	2.4 ± 0.7
Difference (%)	15.3	14.4	4%

$$T = T_0 + \frac{Q}{2\pi R \kappa} \exp \left[\frac{-v(\xi + R)}{2\alpha} \right] \quad 4$$

In Eq. 4, T is the local temperature, T_0 is the building plate temperature, Q is the absorbed power, R is the radial distance to the laser beam, κ is the thermal conductivity, v is the beam velocity, ξ is the distance to the beam in laser traveling direction, and α is the thermal diffusivity. The cooling rate can be derived from Rosenthal equation as expressed in Eq. 5:

$$\dot{T} = 2\pi\kappa(T_s - T_0)(T_L - T_0) \frac{v}{Q} \quad 5$$

where \dot{T} is the cooling rate, T_s and T_L are the solidus and liquidus temperatures, respectively. To estimate the cooling rate, we approximate the thermal conductivity of our customized Al alloy as that of AlSi₁₀Mg, where $\kappa_{powder} = 150 \text{ W/m} \cdot \text{K}$ [41] and $\kappa_{bulk} = 233 \text{ W/m} \cdot \text{K}$ [42]. Solidus and liquidus temperatures were simulated by ThermoCalc Scheil calculation $T_s = 912 \text{ K}$ and $T_L = 1345 \text{ K}$, T_0 and v are different for laser-scanned and 3D-printed samples (refer to Table 2), and the absorbed power Q is determined as the product of the absorption coefficient (estimated at 0.35 for AlSi₁₀Mg [41]) and the laser power which differs between the two samples (refer to Table 2). Consequently, the theoretical cooling rate for the laser-scanned sample is computed to be $\dot{T}_{laser} = 2.0 \times 10^6 \text{ K/s}$, while for the 3D-printed sample, it is $\dot{T}_{3D} = 3.2 \times 10^6 \text{ K/s}$ falling within the same magnitude. Despite the smaller scanning speed and laser power employed for the 3D-printed sample, which could have resulted in a much larger cooling rate, the preheated build plate to 200°C mitigates the temperature gradient, thereby resulting in the same magnitude cooling rate to that of the laser-scanned sample. The smaller cooling rate for the laser-scanned sample could account for its slightly larger phase size. Nonetheless, the difference in phase size is considerably small and the microstructural morphology and phase distribution remain consistent between the two samples, especially when we increased the magnification.

The hardness of the two specimens is shown in Table 4.

Table. 4 Microhardness comparison between the two sample

	Hardness (HV)
3D-printed sample	200.42 ± 21.6
Laser-scanned sample	158.61 ± 24.1
Difference (%)	20.5

To measure the hardness of the laser-scanned sample, we followed the general indentation rule for thin film samples that the indentation depth must be within 10% of film thickness to reduce the substrate effect [43], [44]. In this case, laser-scanned regions are analogous to thin-film which has fine microstructure and different mechanical properties to the unscanned region which can be analogous to the substrate. The average indentation depth is ~7 μm which is within 10% of the multi-path melt pool depth of ~250 μm. Thus, the hardness safely reflects the property in the laser-scanned region. Despite the similarity in microstructure, the laser-scanned sample exhibited a hardness that was 20% lower than that of the 3D-printed counterpart. There are two potential reasons:

1). The phase fraction of the strengthening phases could be different. According to Eq. 3, Orowan strengthening depends on both precipitates size and phase fractions. However, in this material system, the precipitates phase fraction is very difficult to measure. The crystallography information of the ternary $\text{Al}_{23}\text{Ni}_6\text{Er}_4$ metastable phase is still undocumented in literature and material databases. More TEM work needs to be done to characterize its crystal structure. Besides, the precipitates phase size is so small in nanometer size. All these factors make it hard for laboratory X-ray diffraction as a general approach to phase fraction characterization.

2). In LPBF printing, the cyclical thermal exposure along the build direction induces a transformation from the metastable ternary phase to L_{12} phase (see Fig. 7, less Er on grain boundaries of the 3D-printed sample in Fig. 4). The L_{12} phase, characterized by its nanometer size, enhances material strength through the Orowan mechanism (Eq. 2). Consequently, the increased presence of the L_{12} phase accounts for the elevated hardness observed in the 3D-printed sample.

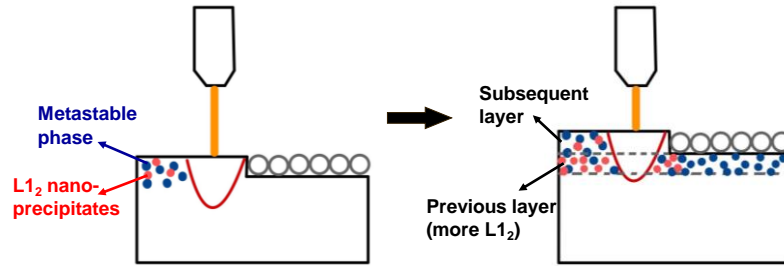


Fig. 7 Schematic of LPBF. The cyclic thermal history parallel to building direction facilitate the transformation of metastable phase formed in the previous layer into L_{12} nanoprecipitates which enhance the material hardness.

One may argue that the difference in hardness results from the different phase sizes of Al grain and ternary precipitates. However, based on the Hall Petch (Eq. 1) and Orowan strengthening (Eq. 2) equations, such ~15% differences become even less (~5%) after taking the square root. Besides, according to the two strengthening mechanisms, it is evident that the dominance in strength is governed by precipitates of smaller dimensions—specifically, the L_{12} nanoprecipitates in our samples. The contributions of the two strengthening mechanisms at in-service conditions (equilibrium state at 250°C) were estimated by employing Eq. 1 and Eq. 2. Since it is at high temperature equilibrium state, all metastable ternary phase will transform into L_{12} phase, thus the Orowan strengthening is mainly from L_{12} nanoprecipitates with a phase fraction of $f = 0.033$ from ThermoCalc simulation as shown in Table. 1. By taking $Q = 3.06$ [45], $G = 25.4$ GPa [46], $b = 0.286$ nm, and $\nu = 0.345$ [45] for pure Al, the theoretical contribution of Orowan strengthening is ~600 MPa. However, the contribution of grain boundary strengthening is only ~40 MPa by taking $\sigma_0 = 11$ MPa and $K = 0.044$ $\text{MPa} \cdot \sqrt{\text{m}}$ for pure Al with a grain size of 3 – 11 μm [47] (our Al grain size falls into this range). Thus, despite the observed slight increase in size for Al grains and ternary precipitates, the contribution to the strength is much smaller compared to that from the 2-5 nm L_{12} nanoprecipitates.

To validate our methodology, we also compared the hardness of the laser-scanned and 3D-printed sample of a printable benchmark alloy (Al-Ni-Zr-Er-Y-Yb) [11]. The 3D-printed

sample and the laser-scanned sample of the benchmark alloy were prepared in an identical approach to the model alloy. Initially, we found our additively manufactured sample has 52% higher hardness than the benchmark. Then, we found that the laser-scanned samples with the same processing parameters can nearly reproduce such hardness enhancement showcasing a 54% increase for our alloy. Furthermore, the hardness variance due to different processing in our designed alloy was also observed in the benchmark alloy. As illustrated in Fig. 8, for our designed alloy, the 3D-printed sample demonstrated a 21% increase in microhardness relative to its laser-scanned counterpart. A comparable trend was observed for the benchmark alloy, with a 22% augmentation in microhardness for the 3D-printed sample, demonstrating a 1% absolute error compared with our model alloy. The independence of two different alloys reveals the potential to be applied to other material systems.

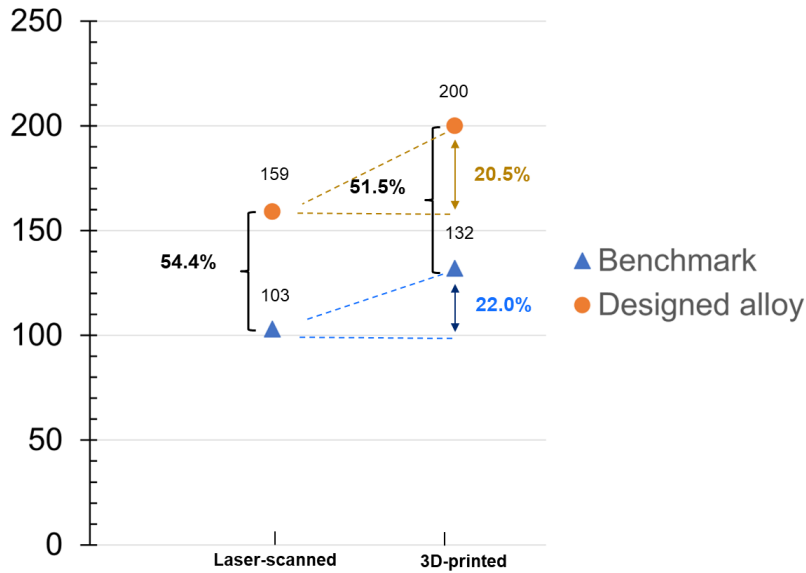


Fig. 8 Comparison of the microhardness between Taheri-Mousavi alloy and benchmark alloy for both laser-scanned sample and 3D-printed sample.

The outcomes of this study hold promise for advancing alloy design within the realm of AM. The observed parallels in microstructure and the relative representativeness in hardness between laser-scanned and additively manufactured samples offer an advantage in circumventing powder production as a primary bottleneck of alloy design. Utilizing laser-scanned samples can effectively expedite the iterative design process, providing a cost-effective and rapid means of screening compositions. For instance, in the context of designing a creep-resistant alloy, the hardness trends observed in laser-scanned alloys at varying temperatures can serve as indicative markers. If, for instance, a decrease in hardness is noted with increasing temperatures, it becomes highly probable that such a composition may not be a viable candidate. However, limitations indeed exist in this work. The laser parameters were restricted to values where maximum density was achieved for both samples. Furthermore, this investigation primarily focused on comparing two alloy systems, predominantly centered on Al alloys. Our future work will extend the research on additional alloy systems and will incorporate varying processing parameters and their interplay with melt pool behavior. This study instead aims to spark an inspiration that laser-scanned samples can serve as valuable tools for down-selecting promising designs of powder-based alloys under specific conditions. This, in turn, encourages broader exploration into

different laser parameters and alloy systems to enrich the knowledge of alloy design in AM community.

5. Conclusion

To address the constrained availability of powder for customized alloys in the powder-based AM field, this paper used Al-Ni-Zr-Er as a model alloy to investigate how much a laser-scanned cast sample, as a rapid experimental workflow aimed at mimicking rapid solidification of AM, can be representative of LPBF sample. There are several major conclusions:

- a. At a low magnification scale ($\times 5000$ magnification), both samples have a dual-morphology microstructure of eutectic lamellar and equiaxed grains. Zr-rich phase was found to be larger in the laser-scanned sample. The phenomenon was explained by the incomplete remelting of the phase in the induction-melted sample which is larger than the beam size.
- b. At middle magnification scale ($\times 12000$ magnification), Er-rich phase was found to be more segregated at Al grain boundaries in the laser-scanned sample. The reason was discussed to be the thermal cycle in 3D-printed samples enables more transformation from locally segregated metastable ternary phase into dispersed nanoscale $L1_2$ precipitates inside Al grains.
- c. At a high magnification scale ($\times 80000$ magnification), microstructure morphology, phase distribution, and phase size were highly resembled. At atomic scale, $L1_2$ nanoprecipitates with the same core-shell structure were observed in both samples.
- d. In the laser-scanned sample, Al grains and ternary precipitates were 15% and 14% larger than those in the 3D-printed sample, while $L1_2$ nanoprecipitate size remains only 4% differences between the two samples.
- e. Vicker's hardness test was performed on the as-print surface of both samples. The laser-scanned sample manifests a hardness 20% lower than that of the 3D-printed sample. Two potential reasons were discussed: 1). Phase fractions were difficult to characterize and could be different; 2). Cyclic thermal history during powder processing causes metastable phase transformation into strengthening $L1_2$ phase.
- f. The hardness test was repeated to the 3D-printed and laser-scanned sample of the benchmark alloy. The two samples were prepared in the identical method with the model alloy. The laser-scanned sample exhibited a consistent amount of decrease in hardness compared with its corresponding 3D-printed sample with only 1% absolute difference, demonstrating a relative representativeness to the AM sample in hardness.

The study contends that the observed consistency in microstructure and relative representativeness in hardness is deemed sufficient to yield informative insights to validate the composition from alloy design in powder-based AM field while acknowledging the limitations in the scope of laser parameters and material system. This can be used to down-select compositions from broad compositional space for further analyses.

Credit authorship contribution statement:

Zhaoxuan Ge: Writing – Original Draft, Data curation, Formal analysis, Validation, Investigation. **Calderon Sebastian:** Data curation, Software, Writing – Review & Editing. **S. Mohadeseh Taheri-Mousavi:** Conceptualization, Methodology, Supervision, Writing – Review & Editing, Funding acquisition.

Acknowledgements:

The author extends gratitude to Florian Hengsbach for the induction melting, laser-scanning, and printing of the sample, and to James M. LeBeau and Michael Xu for their diligent efforts in characterizing the 3D-printed sample. Special appreciation is also extended to Shaoulou Wei for his fruitful discussions, reviewing, and advising on the paper manuscript. We would also like to thank AMAZEMENT company for making all the powder.

Funding sources:

The support for this research was provided by the Army Research Lab under Grant No. W911NF-20-2-0175. This research (or “A portion of this research”) was sponsored by the Army Research Laboratory and was accomplished under Cooperative Agreement Number W911NF-20-2-0175. The views and conclusions contained in this document are those of the authors and should not be interpreted as representing the official policies, either expressed or implied, of the Army Research Laboratory or the U.S. Government. The U.S. Government is authorized to reproduce and distribute reprints for Government purposes notwithstanding any copyright notation herein

Supplementary information:

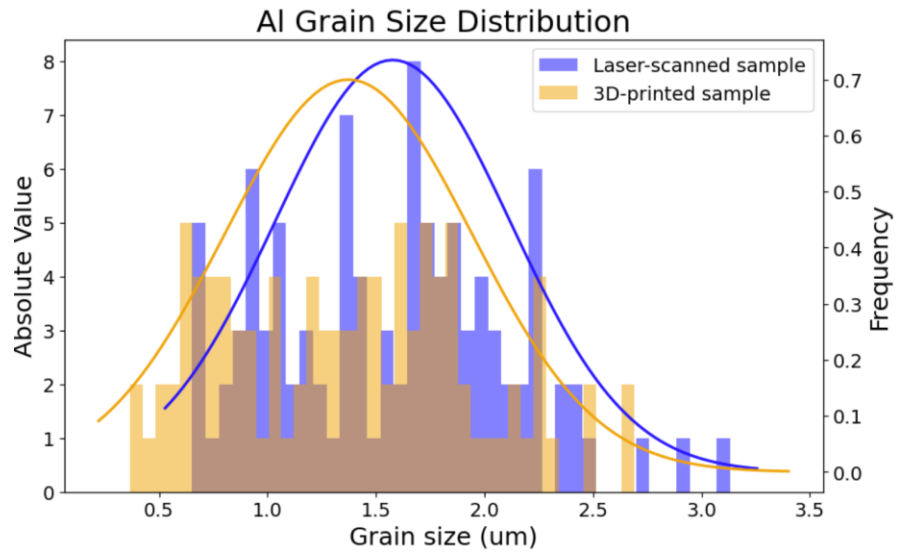


Fig. S1 Al grain size distribution in laser-scanned and 3D-printed sample. A total of 100 data were collected for both samples.

Reference:

- [1] H. Hyer, L. Zhou, A. Mehta, and Y. Sohn, 'Effects of Alloy Composition and Solid-State Diffusion Kinetics on Powder Bed Fusion Cracking Susceptibility', *J Phase Equilibria Diffus*, vol. 42, no. 1, pp. 5–13, Feb. 2021, doi: 10.1007/s11669-020-00844-y.
- [2] K. G. Prashanth *et al.*, 'Microstructure and mechanical properties of Al–12Si produced by selective laser melting: Effect of heat treatment', *Materials Science and Engineering: A*, vol. 590, pp. 153–160, Jan. 2014, doi: 10.1016/j.msea.2013.10.023.
- [3] C. J. Hung *et al.*, 'Novel Al-X alloys with improved hardness', *Mater Des*, vol. 192, p. 108699, Jul. 2020, doi: 10.1016/j.matdes.2020.108699.
- [4] N. Takata, M. Liu, H. Kodaira, A. Suzuki, and M. Kobashi, 'Anomalous strengthening by supersaturated solid solutions of selectively laser melted Al–Si-based alloys', *Addit Manuf*, vol. 33, p. 101152, May 2020, doi: 10.1016/j.addma.2020.101152.
- [5] K. G. Prashanth and J. Eckert, 'Formation of metastable cellular microstructures in selective laser melted alloys', *J Alloys Compd*, vol. 707, pp. 27–34, Jun. 2017, doi: 10.1016/j.jallcom.2016.12.209.
- [6] X. P. Li *et al.*, 'A selective laser melting and solution heat treatment refined Al–12Si alloy with a controllable ultrafine eutectic microstructure and 25% tensile ductility', *Acta Mater*, vol. 95, pp. 74–82, Aug. 2015, doi: 10.1016/j.actamat.2015.05.017.
- [7] J. Wu, X. Q. Wang, W. Wang, M. M. Attallah, and M. H. Loretto, 'Microstructure and strength of selectively laser melted AlSi10Mg', *Acta Mater*, vol. 117, pp. 311–320, Sep. 2016, doi: 10.1016/j.actamat.2016.07.012.
- [8] A. B. Spierings, K. Dawson, M. Voegtlin, F. Palm, and P. J. Uggowitzer, 'Microstructure and mechanical properties of as-processed scandium-modified aluminium using selective laser melting', *CIRP Annals*, vol. 65, no. 1, pp. 213–216, 2016, doi: 10.1016/j.cirp.2016.04.057.
- [9] A. Plotkowski *et al.*, 'Evaluation of an Al-Ce alloy for laser additive manufacturing', *Acta Mater*, vol. 126, pp. 507–519, Mar. 2017, doi: 10.1016/j.actamat.2016.12.065.
- [10] R. A. Michi, A. Plotkowski, A. Shyam, R. R. Dehoff, and S. S. Babu, 'Towards high-temperature applications of aluminium alloys enabled by additive manufacturing', *International Materials Reviews*, vol. 67, no. 3. Taylor and Francis Ltd., pp. 298–345, 2022. doi: 10.1080/09506608.2021.1951580.
- [11] J. Gong, G. B. Olson, D. R. Snyder, and T. S. Kozmel II, 'Multicomponent aluminum alloys for applications such as additive manufacturing', PCT/US2018/062761, 2019
- [12] S. Mohadeseh Taheri-Mousavi, Anastasios Hart, and Greg Olson, 'Methodologies for formulating compositions, including aluminum alloys with high-temperature strength', WO 2024/092273 A2, 2024
- [13] S. Mohadeseh Taheri-Mousavi *et al.*, 'Additively manufacturable high-strength aluminum alloys with thermally stable microstructures enabled by hybrid machine learning-based design', *Science (1979)*, 2024.

- [14] A. Bandyopadhyay, K. D. Traxel, M. Lang, M. Juhasz, N. Eliaz, and S. Bose, 'Alloy design via additive manufacturing: Advantages, challenges, applications and perspectives', *Materials Today*, vol. 52. Elsevier B.V., pp. 207–224, Jan. 01, 2022. doi: 10.1016/j.mattod.2021.11.026.
- [15] S. A. Kube, S. Sohn, D. Uhl, A. Datye, A. Mehta, and J. Schroers, 'Phase selection motifs in High Entropy Alloys revealed through combinatorial methods: Large atomic size difference favors BCC over FCC', *Acta Mater*, vol. 166, pp. 677–686, Mar. 2019, doi: 10.1016/j.actamat.2019.01.023.
- [16] B. E. Carroll *et al.*, 'Functionally graded material of 304L stainless steel and inconel 625 fabricated by directed energy deposition: Characterization and thermodynamic modeling', *Acta Mater*, vol. 108, pp. 46–54, Apr. 2016, doi: 10.1016/j.actamat.2016.02.019.
- [17] D. R. Feenstra, R. Banerjee, H. L. Fraser, A. Huang, A. Molotnikov, and N. Birbilis, 'Critical review of the state of the art in multi-material fabrication via directed energy deposition', *Curr Opin Solid State Mater Sci*, vol. 25, no. 4, p. 100924, Aug. 2021, doi: 10.1016/j.cossms.2021.100924.
- [18] M. Ansari, E. Jabari, and E. Toyserkani, 'Opportunities and challenges in additive manufacturing of functionally graded metallic materials via powder-fed laser directed energy deposition: A review', *J Mater Process Technol*, vol. 294, p. 117117, Aug. 2021, doi: 10.1016/j.jmatprotec.2021.117117.
- [19] W. Li *et al.*, 'Comprehensive studies of SS316L/IN718 functionally gradient material fabricated with directed energy deposition: Multi-physics & multi-materials modelling and experimental validation', *Addit Manuf*, vol. 61, p. 103358, Jan. 2023, doi: 10.1016/J.ADDMA.2022.103358.
- [20] C. S. Lefky, B. Zucker, A. R. Nassar, T. W. Simpson, and O. J. Hildreth, 'Impact of compositional gradients on selectivity of dissolvable support structures for directed energy deposited metals', *Acta Mater*, vol. 153, pp. 1–7, Jul. 2018, doi: 10.1016/J.ACTAMAT.2018.04.009.
- [21] R. Zhang, N. Bian, H. Lu, Y. Li, Y. Tian, and W. Li, 'Molten pool swing in printing the steel/inconel functionally gradient material with laser-based Directed Energy Deposition', *Manuf Lett*, vol. 32, pp. 44–48, Apr. 2022, doi: 10.1016/J.MFGLET.2022.03.002.
- [22] M. A. S. R. Saadi *et al.*, 'Direct Ink Writing: A 3D Printing Technology for Diverse Materials', *Advanced Materials*, vol. 34, no. 28, Jul. 2022, doi: 10.1002/adma.202108855.
- [23] M. R. Alkahari, T. Furumoto, T. Ueda, and A. Hosokawa, 'Melt Pool and Single Track Formation in Selective Laser Sintering/Selective Laser Melting', *Adv Mat Res*, vol. 933, pp. 196–201, May 2014, doi: 10.4028/www.scientific.net/AMR.933.196.
- [24] A. K. Mishra and A. Kumar, 'Effect of surface morphology on the melt pool geometry in single track selective laser melting', *Mater Today Proc*, vol. 27, pp. 816–823, Jan. 2020, doi: 10.1016/J.MATPR.2019.12.357.
- [25] S. Ghosh *et al.*, 'Single-Track Melt-Pool Measurements and Microstructures in Inconel 625', *JOM*, vol. 70, no. 6, pp. 1011–1016, Jun. 2018, doi: 10.1007/s11837-018-2771-x.
- [26] S. Shrestha and K. Chou, 'Single track scanning experiment in laser powder bed fusion process', *Procedia Manuf*, vol. 26, pp. 857–864, Jan. 2018, doi: 10.1016/J.PROMFG.2018.07.110.

- [27] C. Tang, J. L. Tan, and C. H. Wong, 'A numerical investigation on the physical mechanisms of single track defects in selective laser melting', *Int J Heat Mass Transf*, vol. 126, pp. 957–968, Nov. 2018, doi: 10.1016/J.IJHEATMASSTRANSFER.2018.06.073.
- [28] J. C. Heigel and B. M. Lane, 'Measurement of the Melt Pool Length During Single Scan Tracks in a Commercial Laser Powder Bed Fusion Process', *J Manuf Sci Eng*, vol. 140, no. 5, May 2018, doi: 10.1115/1.4037571.
- [29] I. Yadroitsev, A. Gusarov, I. Yadroitsava, and I. Smurov, 'Single track formation in selective laser melting of metal powders', *J Mater Process Technol*, vol. 210, no. 12, pp. 1624–1631, Sep. 2010, doi: 10.1016/J.JMATPROTEC.2010.05.010.
- [30] P. B. Hirsch and F. J. Humphreys, *Plastic deformation of two-phase alloys containing small nondeformable particles*. Cambridge, MA: MIT Press, 1969.
- [31] Eckhard Nembach, *Particle Strengthening of Metals and Alloys*, 1st ed. New York: Wiley-VCH, 1997.
- [32] X. Sang and J. M. LeBeau, 'Revolving scanning transmission electron microscopy: Correcting sample drift distortion without prior knowledge', *Ultramicroscopy*, vol. 138, pp. 28–35, Mar. 2014, doi: 10.1016/j.ultramic.2013.12.004.
- [33] A. B. Yankovich *et al.*, 'Non-rigid registration and non-local principle component analysis to improve electron microscopy spectrum images', *Nanotechnology*, vol. 27, no. 36, p. 364001, Sep. 2016, doi: 10.1088/0957-4484/27/36/364001.
- [34] W. Nasim *et al.*, 'Structure and growth of core-shell nanoprecipitates in Al–Er–Sc–Zr–V–Si high-temperature alloys', *J Mater Sci*, vol. 54, no. 2, pp. 1857–1871, Jan. 2019, doi: 10.1007/s10853-018-2941-9.
- [35] K. E. Knipling, D. N. Seidman, and D. C. Dunand, 'Ambient- and high-temperature mechanical properties of isochronally aged Al-0.06Sc, Al-0.06Zr and Al-0.06Sc-0.06Zr (at.%) alloys', *Acta Mater*, vol. 59, no. 3, pp. 943–954, Feb. 2011, doi: 10.1016/j.actamat.2010.10.017.
- [36] C. Zhang, D. Yin, Y. Jiang, and Y. Wang, 'Precipitation of L1 2 -phase nano-particles in dilute Al-Er-Zr alloys from the first-principles', *Comput Mater Sci*, vol. 162, pp. 171–177, May 2019, doi: 10.1016/j.commatsci.2019.03.001.
- [37] C. B. Fuller, D. N. Seidman, and D. C. Dunand, 'Mechanical properties of Al(Sc,Zr) alloys at ambient and elevated temperatures', *Acta Mater*, vol. 51, no. 16, pp. 4803–4814, Sep. 2003, doi: 10.1016/S1359-6454(03)00320-3.
- [38] C. Booth-Morrison, Z. Mao, M. Diaz, D. C. Dunand, C. Wolverton, and D. N. Seidman, 'Role of silicon in accelerating the nucleation of Al₃(Sc,Zr) precipitates in dilute Al–Sc–Zr alloys', *Acta Mater*, vol. 60, no. 12, pp. 4740–4752, Jul. 2012, doi: 10.1016/j.actamat.2012.05.036.
- [39] D. Erdeniz *et al.*, 'Effect of vanadium micro-alloying on the microstructural evolution and creep behavior of Al-Er-Sc-Zr-Si alloys', *Acta Mater*, vol. 124, pp. 501–512, Feb. 2017, doi: 10.1016/j.actamat.2016.11.033.

- [40] D. Rosenthal, 'The Theory of Moving Sources of Heat and Its Application to Metal Treatments', *J Fluids Eng*, vol. 68, no. 8, pp. 849–865, Nov. 1946, doi: 10.1115/1.4018624.
- [41] M. Tang, P. C. Pistorius, S. Narra, and J. L. Beuth, 'Rapid Solidification: Selective Laser Melting of AlSi10Mg', *JOM*, vol. 68, no. 3, pp. 960–966, Mar. 2016, doi: 10.1007/s11837-015-1763-3.
- [42] J. Ning, W. Wang, X. Ning, D. E. Sievers, H. Garmestani, and S. Y. Liang, 'Analytical Thermal Modeling of Powder Bed Metal Additive Manufacturing Considering Powder Size Variation and Packing', *Materials*, vol. 13, no. 8, p. 1988, Apr. 2020, doi: 10.3390/ma13081988.
- [43] X. Chen and J. J. Vlassak, 'Numerical study on the measurement of thin film mechanical properties by means of nanoindentation', *J Mater Res*, vol. 16, no. 10, pp. 2974–2982, Oct. 2001, doi: 10.1557/JMR.2001.0408.
- [44] R. Saha and W. D. Nix, 'Effects of the substrate on the determination of thin film mechanical properties by nanoindentation', *Acta Mater*, vol. 50, no. 1, pp. 23–38, Jan. 2002, doi: 10.1016/S1359-6454(01)00328-7.
- [45] M. A. Meyers and K. K. Chawla, *Mechanical metallurgy — Principles and applications*. Englewood Cliffs: Prentice-Hall, 1984.
- [46] H. J. Frost and M. F. Ashby, *Deformation-mechanism Maps: The Plasticity and Creep of Metals and Ceramics*. New York: Pergamon Press, 1982.
- [47] J. W. Wyrzykowski and M. W. Grabski, 'The Hall–Petch relation in aluminium and its dependence on the grain boundary structure', *Philosophical Magazine A*, vol. 53, no. 4, pp. 505–520, Apr. 1986, doi: 10.1080/01418618608242849.